J. Fluid Mech. (2019), *vol.* 871, *pp.* 305–331.
doi:10.1017/jfm.2019.285

The evolution of the initial flow structures of a highly under-expanded circular jet

Huan-Hao Zhang[1], Nadine Aubry[2], Zhi-Hua Chen[1,†], Wei-Tao Wu[3,†] and Sha Sha[4]

[1]Key Laboratory of Transient Physics, Nanjing University of Science and Technology, Nanjing 210094, China

[2]Department of Mechanical and Industrial Engineering, Northeastern University, Boston, MA 02115, USA

[3]School of Mechanical Engineering, Nanjing University of Science and Technology, Nanjing 210094, China

[4]Beijing Institute of Electronic System Engineering, Beijing 100854, China

(Received 16 May 2018; revised 7 March 2019; accepted 3 April 2019; first published online 20 May 2019)

The three-dimensional flow characteristics of the compressible vortex ring generated by under-expanded circular jets with two typical pressure ratios, i.e. $n = 1.4$ (moderate) and 4.0 (high), are investigated numerically with the use of large-eddy simulations. Our results illustrate that these two pressure ratios correspond to different shock structures (shock cell and Mach disc, respectively) within the jet. These two typical types of flow structures and characteristics are discussed and validated with experiments, and the different generation mechanisms of the secondary vortex rings are compared. Moreover, detailed information about the evolution of the secondary vortex ring, primary vortex ring and turbulence transition features, including the radial and azimuthal modes, is investigated. The geometric features and mixing effects of the jets are also explored.

Key words: gas dynamics, jets, transition to turbulence

1. Introduction

Due to their importance in both fundamental research and engineering applications, compressible vortex rings generated by unsteady supersonic jets have been investigated extensively, and the best-known applications involve supersonic combustion (Hamzehloo & Aleiferis 2016), projectile launch (Zhang *et al.* 2013; Li *et al.* 2015) and propulsion systems (Zhang *et al.* 2011). Accompanying the development of such compressible vortex rings, there are many other important physical phenomena involved, such as the free shear layer, shock wave diffraction, turbulence transition, shock–vortex interaction and aerodynamic noise. Therefore, the study of the growth, instability and breakdown of compressible vortex rings facilitates the understanding of many types of transient flows and compressible turbulence. Many experimental, numerical and

† Email addresses for correspondence: chenzh@njust.edu.cn, weitaowwtw@njust.edu.cn

theoretical investigations have been performed to study the evolution of supersonic jets (Arakeri *et al.* 2004; Maeno *et al.* 2005; Zare-Behtash, Kontis & Gongora-Orozco 2008*a*; Zare-Behtash, Kontis & Takayama 2008*b*; Kitajima, Iwamoto & Tamura 2009; Zare-Behtash *et al.* 2009*a*; Zare-Behtash, Gongora-Orozco & Kontis 2009*b*; Murugan & Das 2010; Zare-Behtash *et al.* 2010; Mariani, Quinn & Kontis 2013). However, very few works have attempted to reveal the mechanisms of the propagation of compressible vortices and their interaction with shock waves when the effects of turbulence and compressibility are important.

According to previous studies, the flow characteristics of a supersonic jet stemming from a circular nozzle are highly dependent on the Mach number and the ratio of the upstream total pressure (p_j) to the ambient static pressure (p_0), specifically the pressure ratio ($n = p_j/p_0$). The Mach number affects the structures of both the trailing jet shear layer and the compressible vortex ring. For a low Mach number, there is no shock wave, and the vortex ring is conventional and characterized by a thin core. With an increase of the Mach number, flow expansion appears to be more significant at the exit during vortex ring formation. At a high Mach number of approximately 1.4, a pair of vortex-induced shocks appears on the opposite sides of the shear layer of the primary vortex core (Hillier 1991), and a rearward-facing shock with a low pressure upstream and a high pressure downstream embeds inside the axial region of the vortex ring. This embedded shock propagates along with the vortex ring and its end connects with the vortex-induced shock pair (Zare-Behtash *et al.* 2008*a*,*b*; Murugan *et al.* 2013). These unstable waves are entrained into the vortex core, which amplifies and turns the vortex ring from laminar into turbulent flow. The turbulent vortex ring is composed of a vortex core with unstable waves, and this vortex core is filled with turbulent vortices (Minota 1998). With an increase of the Mach number to approximately 1.5–1.65 (Brouillette & Hebert 1997; Murugan & Das 2010; Mariani *et al.* 2013), a secondary vortex ring (SVR) with an opposite circulation appears ahead of the primary vortex ring (PVR). It is believed that the embedded facing shock wave results in the formation of a shear layer ahead of the primary vortex loop, which rolls up into an SVR due to the Kelvin–Helmholtz (K–H) instability (Ishii *et al.* 1999; Zare-Behtash *et al.* 2008*a*,*b*; Murugan & Das 2010; Murugan *et al.* 2013). Then, the SVR merges with the PVR because of the mutual interaction during its evolution and becomes a poorly defined vertical structure at a later stage (Brouillette, Tardif & Gauthier 1995). However, our previous studies (Zhang *et al.* 2014) indicated that the generation mechanism of the SVRs by supersonic under-expanded jets at a low pressure ratio ($n = 1.4$) is the rolling up of the shear layer, which is caused by the combination of two slip lines when the two triple points on the embedded shock wave interact with each other. For an under-expanded jet, the pressure at the nozzle exit is still higher than the ambient pressure, and the pressure ratio is the important parameter for measuring the under-expanded level. After formation, the SVR interacts with the PVR and rolls over the periphery of the PVR and moves upstream. For a higher Mach number of 1.8, multiple SVRs form during the evolution.

Depending on the nozzle pressure ratio (Donaldson & Snedeker 1971), the jets can be characterized as follows: (1) subsonic jet, $n = 1$; (2) moderately under-expanded jet, $1.1 < n \leqslant 2$; and (3) highly under-expanded jet, $n > 2$. In moderately under-expanded conditions, the trailing jet flow is observed to display the typical oblique shock pattern (shock diamonds). In highly under-expanded conditions, the oblique shock (barrel shock) terminates at a nearly normal shock (often called the Mach disc), where the triple point is their joint. The Mach reflection produces a reflected shock and a slip line. The slip line shows the existence of an annular shear layer with a

vorticity of opposite rotation and its magnitude is approximately half of that of the main trailing jet. Due to the K–H instability along the slip lines, SVRs are generated ahead of the PVR and orbit around it (Ishii *et al.* 1999). Moreover, analysis of the vorticity field has shown that these secondary vortices have an opposite vorticity to that of the PVR and are approximately half its strength (Mariani *et al.* 2013).

For the impulsive under-expanded flow emerging from the open end of a shock tube, the flow structures of the compressible vortex rings and shock expansion wave were observed by Arakeri *et al.* (2004), Brouillette & Hebert (1997), Ishii *et al.* (1999) and Zare-Behtash *et al.* (2008*a*,*b*, 2009*a*,*b*, 2010). However, since the integral nature of the visualization techniques (shadowgraph, interferometry and schlieren) is based on the density variation, these experimental visualizations cannot show the flow field in detail; therefore the evolution of the three-dimensional (3-D) flow and turbulence characteristics of the compressible vortex ring cannot be well revealed. In this paper, large-eddy simulation (LES) and high-order hybrid numerical methods are employed to numerically analyse the initiation of the 3-D flow field of a supersonic circular jet for two different pressure ratios of 1.4 (moderately under-expanded jet) and 4.0 (highly under-expanded jet). The characteristics of the generation and the propagation of the compressible vortex rings, as well as their instability and transition to turbulence are evaluated and discussed. Moreover, the radial and azimuthal modes of the flow field are investigated by Fourier analysis (Ran & Colonius 2009).

2. Numerical method and physical model

2.1. *Numerical method*

The compressible LES equations can be obtained by Favre filtering the multicomponent compressible Navier–Stokes equations in the Cartesian coordinate system (Zhang *et al.* 2014, 2015, 2017). For closing the multicomponent LES equations, the subgrid terms are modelled using the multi-component LES equations. We choose the recently developed stretched-vortex subgrid-scales (SGS) model for the multicomponent, compressible flow to approach the unresolved subgrid terms (Lombardini *et al.* 2011). The stretched-vortex SGS model was originally proposed for incompressible fluid (Misra & Pullin 1997) and has been extended to compressible flow (Pullin 2000; Kosovic, Pullin & Samtaney 2002; Hill, Pantano & Pullin 2006). In the stretched-vortex SGS model, the subgrid scales are represented by stretched vortices, and the stretched vortex is a physical model for turbulent fine scales, which are assumed to consist of tube-like structures with concentrated vorticity (Lundgren 1982). The stretched-vortex SGS model is designed for simulating turbulent fine scales and is capable of predicting subgrid-scale quantities systematically.

For a supersonic jet (Ishii *et al.* 1999), complex phenomena, such as shock–vortex interactions and turbulent shear flow, appear in the flow; therefore, the spatial and temporal resolution requirements vary greatly. The hybrid numerical method of tuned centred difference-weighted essentially non-oscillatory (TCD-WENO) (Berger & Colella 1989; Hill & Pullin 2004; Deiterding *et al.* 2007; Pantano *et al.* 2007) has been applied successfully for simulating the shock-induced compressible jet flow (Zhang *et al.* 2014, 2015, 2017). In this paper, the derivatives of inviscid fluxes are computed using a hybrid numerical method with a seven-point TCD scheme and a seven-point WENO upwind scheme, which leads to fifth-order precision. Time advancement is achieved with the fourth-order Runge–Kutta method.

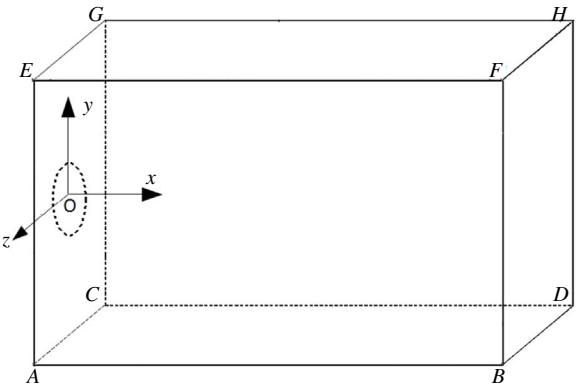

FIGURE 1. Schematic of the computational model.

2.2. *Physical model*

In this paper, a cuboid 3-D computational domain is set up, as shown in figure 1. The length (AB), height (AE) and width (AC) of the computational domain are $Lx = 7.5D$, $Ly = 5.6D$ and $Lz = 5.6D$, respectively. The circular nozzle, with diameter $D = 0.01$ m, is located at the centre of the plane ACGE.

Initially, the gas property within the whole computational domain is set to be uniform with the following parameters: heat ratio $\gamma = 1.4$, dynamic viscosity coefficient $\mu = 1.73 \times 10^{-5}$ Pa s, velocity $u_0 = 0$ (rest), pressure $p_0 = 1.0$ atm and temperature $T = 300$ K. The high-pressure gas is injected into the computational domain from the circular nozzle exit, with a jet Mach number $Ma = 1.8$, and two pressure ratios of jet flow, i.e. $n = p_j/p_0 = 1.4$ or 4.0, are taken as the computational examples. The corresponding Reynolds numbers $Re = \rho_j UD/\mu$ (ρ_j and U are the jet density $\rho_j = p_j/rT$ and velocity $U = Ma \cdot c = Ma \cdot \sqrt{rRT}$, respectively) are 3.6×10^5 and 10.3×10^5, respectively.

To minimize the amplitude of reflective acoustic waves at the boundaries of the computational domain, a combination of non-reflective boundary conditions and sponge outflow is employed at the outflow boundaries (including planes ABFE, CDHG, BDHF, ABDC and EFHG). Moreover, the sponge zone uses spatial low-pass filtering along the x-direction to absorb the waves. These boundary conditions and the numerical scheme are discussed in detail by Colonius, Lele & Moin (1994). On the other hand, the viscous wall boundary condition is applied at the inlet wall ACGE.

A uniform Cartesian grid without cell stretching is used for meshing the computational domain, which typically provides enhanced numerical accuracy and avoids the singularity linked to polar grids. On the other hand, a mesh independency study is performed using several meshes with different resolutions. Figure 2 presents the numerical schlieren images of a moderately under-expanded jet with different meshes; the density, pressure and velocity profiles along the jet's centreline are shown in figure 3. It can be seen in figure 2 that the result obtained using grid numbers of $525 \times 392 \times 392$ is almost the same as that using grid numbers of $675 \times 504 \times 504$. The maximum relative error of all variables between the studied meshes, $525 \times 392 \times 392$ and $675 \times 504 \times 504$, is less than 1 %, and thus we consider the results to be converged. Therefore, in the following, the uniform Cartesian grid number, $525 \times 392 \times 392$, is applied.

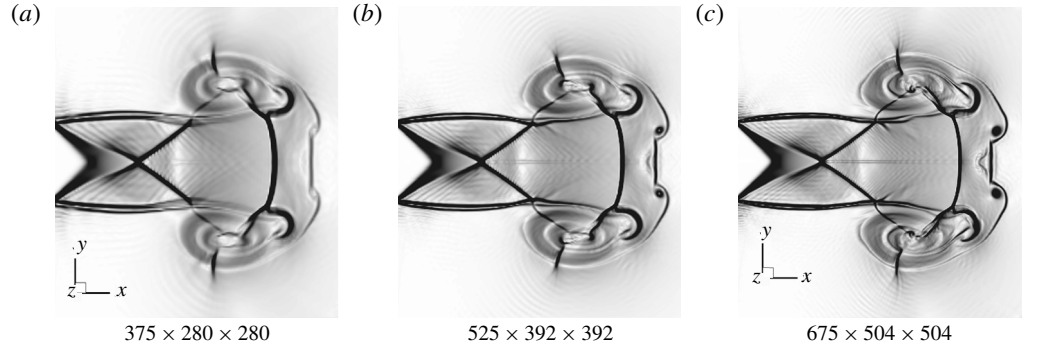

FIGURE 2. The numerical schlieren images of a supersonic jet with different mesh resolutions.

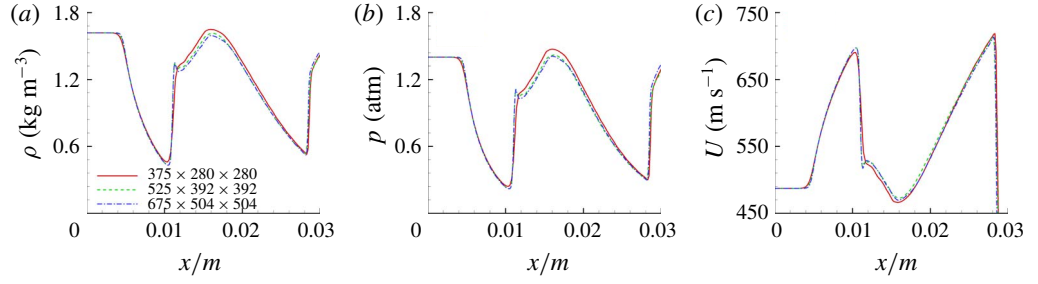

FIGURE 3. (Colour online) The density, pressure and velocity profiles along the symmetric centreline at the same time with different mesh resolutions.

3. Numerical results and discussions

3.1. *Main flow characteristics*

A comparison of the instantaneous numerical schlieren images ($n = 4.0$) and the experimental shadowgraphs ($n = 20.0$) is shown in figure 4. The experimental muzzle flow fields are obtained from our laboratory's previous publication (Li *et al.* 2015). Good agreement between the numerical and experimental results is achieved, and both of them capture the main flow characteristics, such as the Mach disc, vortex-induced shock pair, primary and secondary vortex rings as well as the shock patterns. However, due to different Mach numbers, pressure ratios and environmental perturbations, some particular differences exist. More comparisons between our additional simulation and the corresponding experimental results can be found in Zhang *et al.* (2014, 2017) or in the Appendix.

Figure 5 presents the starting flow structures of under-expanded circular jets at $n = 1.4$ (figure 5*a*, moderately under-expanded jet) and 4.0 (figure 5*b*, highly under-expanded jet). The depictions are obtained from the superimposition of the computational schlieren results of the symmetric plane with the 3-D isosurface of the mixture fraction ($f = 0.85$). It is obvious that the main initial flow structures of both jets include the precursor shock wave, PVR, jet flow (including shear layer), Mach cone, SVR, vortex-induced shock pair, etc. However, due to the different

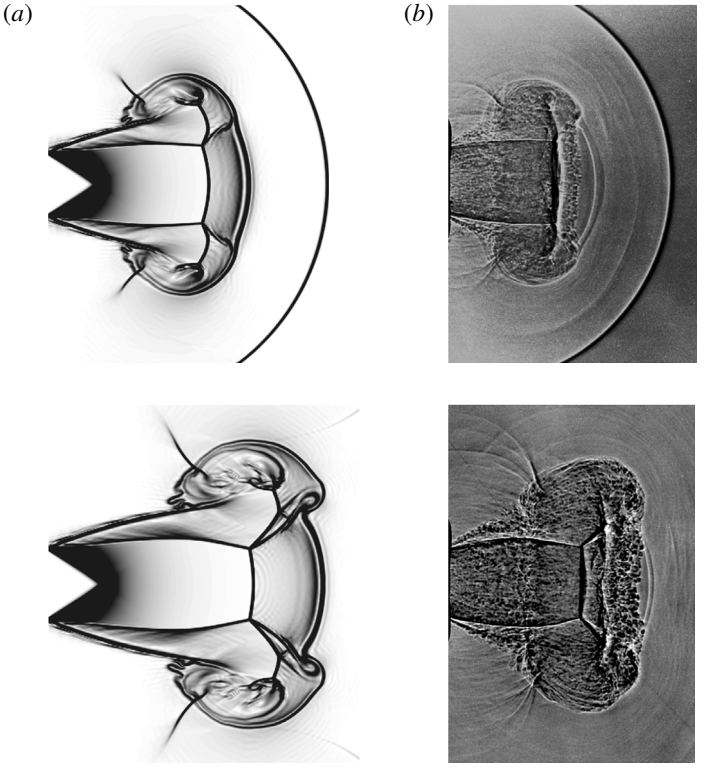

FIGURE 4. Comparison of the instantaneous flow fields of our numerical results with experimental observations (Li *et al.* 2015).

pressure ratios, the shock patterns within the jets are obviously different; therefore, the generation mechanisms of their SVRs are dissimilar.

For the moderately under-expanded jet ($n = 1.4$, figure 5*a*), its pressure ratio is not high enough, and a jet flow with a typical oblique shock pattern (shock cell) is generated behind the PVR. With the growth of the pressure ratio (n), the jet boundary expands to compensate for the higher pressure gradient with respect to the surrounding gas. When the value of n is above the threshold ($n \geqslant 2$) (Matsuda *et al.* 2013), the regular reflection within the trailing jet transits to the Mach reflection. At this moment, the barrel shock appears, it terminates at a triple point (Tp_1) and is followed by the development of a nearly vertical or normal shock known as the Mach disc.

As shown in figure 5(*b*), the barrel shock acts similar to an incident shock wave and its reflection shock wave connects with the first vortex-induced shock pair (VS_1). It is also interesting to observe that the slip line (S_1) starts from the triple points at the Mach disc. The present visualization agrees well with previous experimental schlieren images (Ishii *et al.* 1999; Mariani *et al.* 2013), particularly the shock structures shown in Mariani *et al.* (2013).

Figure 6 illustrates the corresponding normalized transverse and axial velocity profiles along the y axis at different cross-sections ($x/D = 1.0$, 2.0, 3.6 and 4.0). The vorticity and velocity vector fields of the symmetric plane for both jets are shown in figure 7, in which the vector length is proportional to the velocity magnitude.

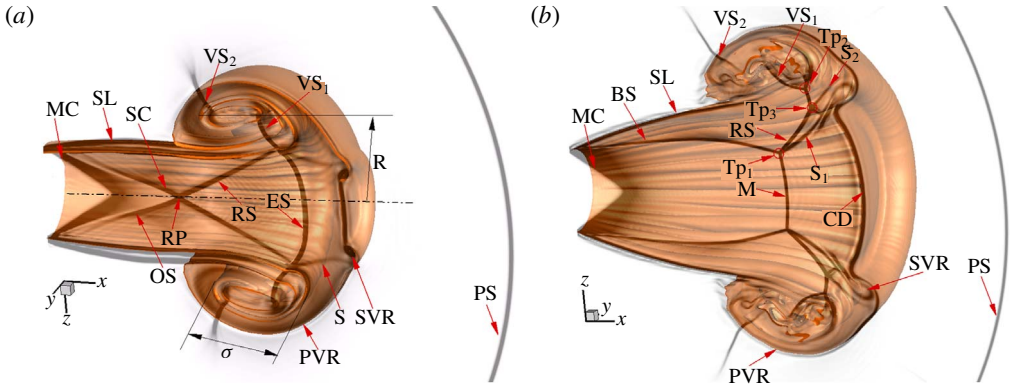

Moderately under-expanded jet ($n = 1.4$) Highly under-expanded jet ($n = 4.0$)

FIGURE 5. (Colour online) The initial flow structures of the supersonic jets for two flow regimes at $t = 0.11$ ms. (BS, barrel shock; CD, cap flow discontinuity; ES, embedded shock; M, Mach disc; MC, Mach cone; OS, oblique shock wave; PS, precursor shock wave; PVR, primary vortex ring; S, S_1, S_2, slipstream; SC, shock cell; SL, shear layer; SVR, secondary vortex ring; RP, reflection point; RS, reflected shock; Tp_1, Tp_2, Tp_3, triple point; VS_1, VS_2, vortex-induced shock pair.)

Following the precursor shock wave, high-pressure gas at the exit characterizes the rapid flow expansion (or Prandtl–Meyer expansion) around the nozzle lip and generates the cone-shaped flow area at the nozzle exit, often referred as the Mach cone. The flow velocities within the Mach cone are the same as the exit velocities, as shown in figure 7. Due to the expansion effects, the high-pressure supersonic gas is accelerated to be at an even higher Mach number along its symmetric axis. Here, the highest Mach number is close to 3.03 for $n = 1.4$ at the first shock reflection point and is 4.90 for $n = 4.0$ in the vicinity of the Mach disc (figure 8).

Based on our simulation results, for $n = 1.4$, the locations of shock reflection points are at $x/D = 1.4$ (first) and 3.6 (second). While for $n = 4.0$, the Mach disc location is at $x/D = 3.0$. The transverse velocity of figure 6 shows that the flow upstream ($x/D = 1.0$) of the first reflection point ($n = 1.4$, $x/D = 1.4$) or Mach disc ($n = 4.0$, $x/D = 3.0$) has a transverse velocity component towards the jet boundary, and the normalized values for $n = 4.0$ are higher than those for $n = 1.4$. Due to the rapid flow expansion, the value of the transverse velocity increases first with distance away from the jet centreline. However, after a radial distance of $y \sim 0.2D$ for $n = 1.4$ and $y \sim 0.5D$ for $n = 4.0$, the flow expansion decreases, and after $y \sim 0.7D$ for $n = 1.4$ and $y \sim 0.9D$ for $n = 4.0$, the velocity turns inwards by passing through an oblique shock wave ($n = 1.4$) or the barrel shock wave ($n = 4.0$). This results in a small transverse velocity component towards the jet centreline, as shown in figure 7. Additionally, the transverse velocity grasp of figure 6 also shows that the flow has a negative transverse velocity after the reflection point ($n = 1.4$, $x/D = 2.0$ and 4.0) or Mach disc ($n = 4.0$, $x/D = 3.6$ and 4.0).

Each axial velocity profile of the moderately under-expanded jet has a section with almost vertical lines for $u/U > 1.0$, which means that the flow along the centreline is accelerated. In addition, the axial velocity component at $x/D = 1.0$ and 3.6 is larger than that at $x/D = 2.0$ and 4.0; this outcome also indicates that the flow accelerates upstream and decelerates downstream of the reflected point.

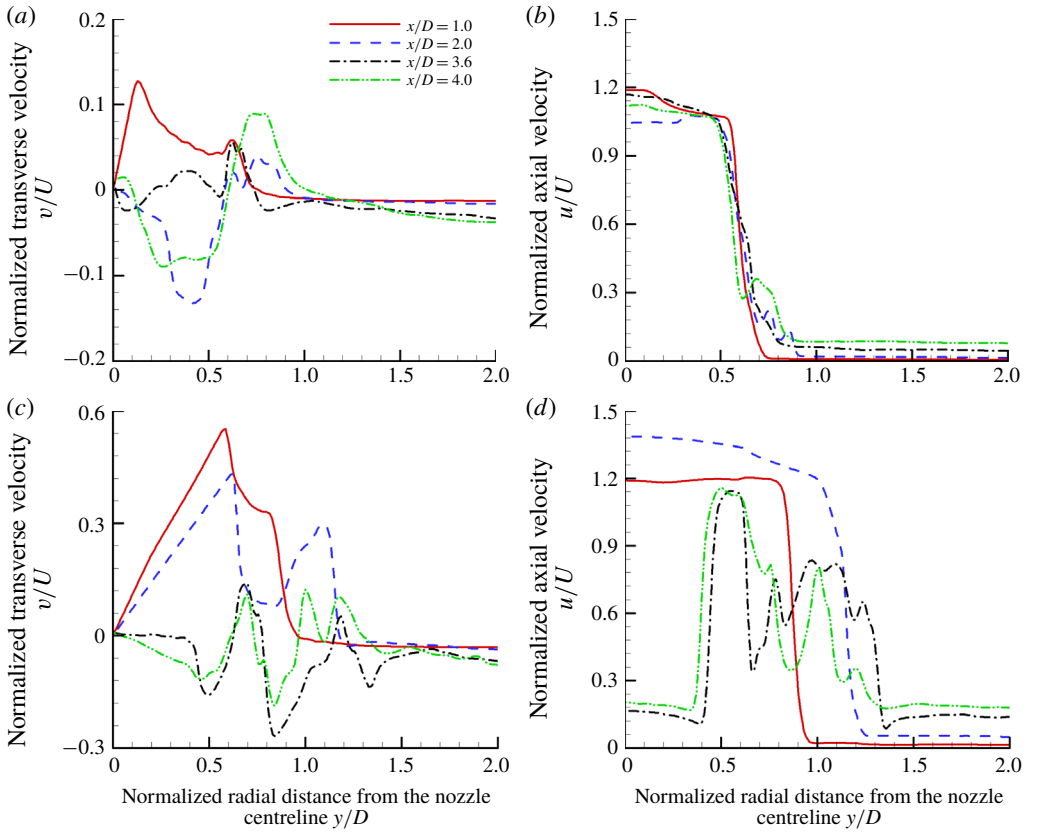

FIGURE 6. (Colour online) Normalized transverse (*a*,*c*) and axial (*b*,*d*) velocity profiles for moderately under-expanded ($n = 1.4$) and highly under-expanded ($n = 4.0$) jets at $t = 0.11$ ms.

On the other hand, the thickness of the jet shear layer can be measured by the distance between the highest y/D of the aforementioned vertical section of the axial velocity and the position where u/U becomes almost zero (Hamzehloo & Aleiferis 2016). It is clear from figure 6(*a*,*c*) that the thickness of the jet shear layer for the moderately under-expanded jet is almost constant. For the highly under-expanded jet, the axial velocity accelerates upstream of the Mach disc and decelerates to subsonic downstream of the Mach disc. Moreover, the thickness of the jet shear layer increases from $x/D = 1.0$ to 2.0 (figure 6*b*,*d*).

The pressure, temperature, density and Mach number distributions along the nozzle centreline for different pressure ratios, $n = 1.0$, 1.4, 2.7 and 4.0, are presented in figure 8. It is clear that the higher the pressure ratio, the greater the density of jet flow issuing from the nozzle exit (figure 8*a*), but the Mach number remains constant at the nozzle exit (figure 8*b*, $Ma = 1.8$). Attributed to the rapid expansion, the higher-pressure supersonic gas is accelerated to an even greater Mach number along the nozzle centreline and reaches the maximum value just upstream of the Mach disc. Correspondingly, its pressure, temperature and density decrease and reach the minimum values (figure 8*a*,*c*,*d*). It can be quantitatively seen that the maximum values of the Mach numbers are equal to 3.03, 4.46 and 4.92 and the minimum

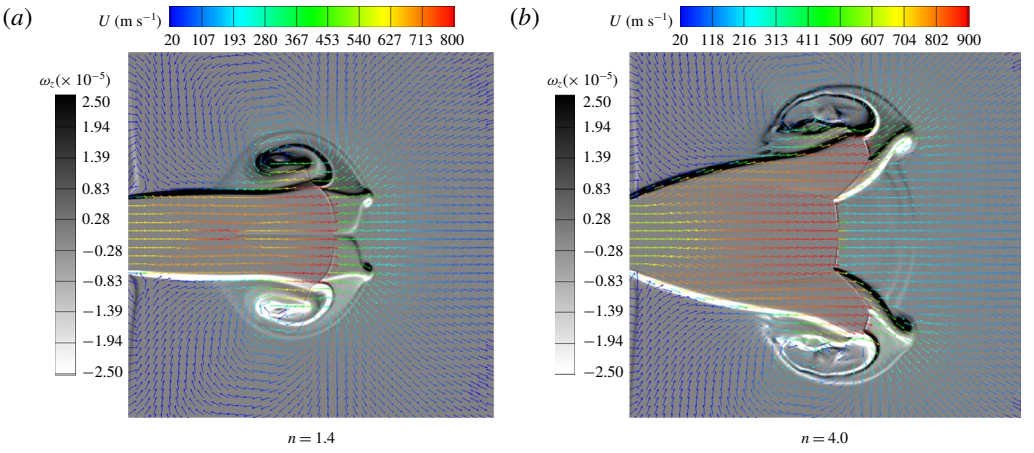

FIGURE 7. (Colour online) Vorticity (ω_z) and velocity vector distribution of the symmetric plane for both jets at $t = 0.11$ ms.

temperature values are equal to 173.1, 101.0 and 84.5 K for $n = 1.4$, 2.7 and 4.0, respectively. According to the quantitative results, the main factor influencing the distribution of the Mach number is the pressure ratio.

3.2. *Evolution of the PVR*

To describe the 3-D evolution of the PVR for different flow regimes, the sequential isosurfaces of the mixture fraction ($f = 0.83$) for the moderately ($n = 1.4$) and highly ($n = 4.0$) under-expanded jets are presented in figures 9 and 10, respectively. The images in figures 9 and 10 have the same scales. Due to the constant azimuthal curvature of the circular nozzle, the flow expands uniformly in all directions, and the primary vortex core appears to have a ring-like pattern. At this stage, the shear layer of the vortex ring belongs to laminar flow, as shown in figures 9(*a*) and 10(*a*). This large vortex ring moves downstream and expands immediately by entraining the ambient gas into its core, which causes a rapid increase of the diameter. Meanwhile, the interactions of the vortex-induced shock pair (VS_1 and VS_2) with the shear layer of the PVR (figure 5) accelerate the instability of the vortex ring (Zhang *et al.* 2015); thus, waviness occurs on the isomixture fraction surface of the vortex core, as shown in figures 9(*c*) and 10(*b*). Then, the vortex core rapidly loses its stability, but the outer interface remains stable (figures 9*d* and 10*c*). Another interesting phenomenon in figures 9(*c*) and 10(*c*) is that the appearance of the coaxial SVR with an opposite circulation presents ahead of the PVR. It interacts with the front interface of the PVR and leads to the deceleration and rolling up of the PVR.

To visualize the small-scale structures, the isosurface of the second invariant Q of the velocity gradient tensor (Hunt, Wray & Moin 1988) is shown in figures 11 and 12; the colour refers to the magnitude of the mixture fraction (f). For the moderately under-expanded jet, the first SVR (figure 11*a*, V_1) remains stable and the identity is distinct after its generation. When V_1 moves near the shear layer of the PVR, its motion is dominated by the PVR because of the large circulation of the PVR. Then, V_1 begins to lose its stability (figure 9*e* and 11*b*) and finally transforms into the irregular waviness at the wake (figure 11*c*, V_1). During the whole process, the size of the first SVR is almost constant. Later, the subsequent SVRs (figure 11*b*,*c*, V_2–V_4), which are

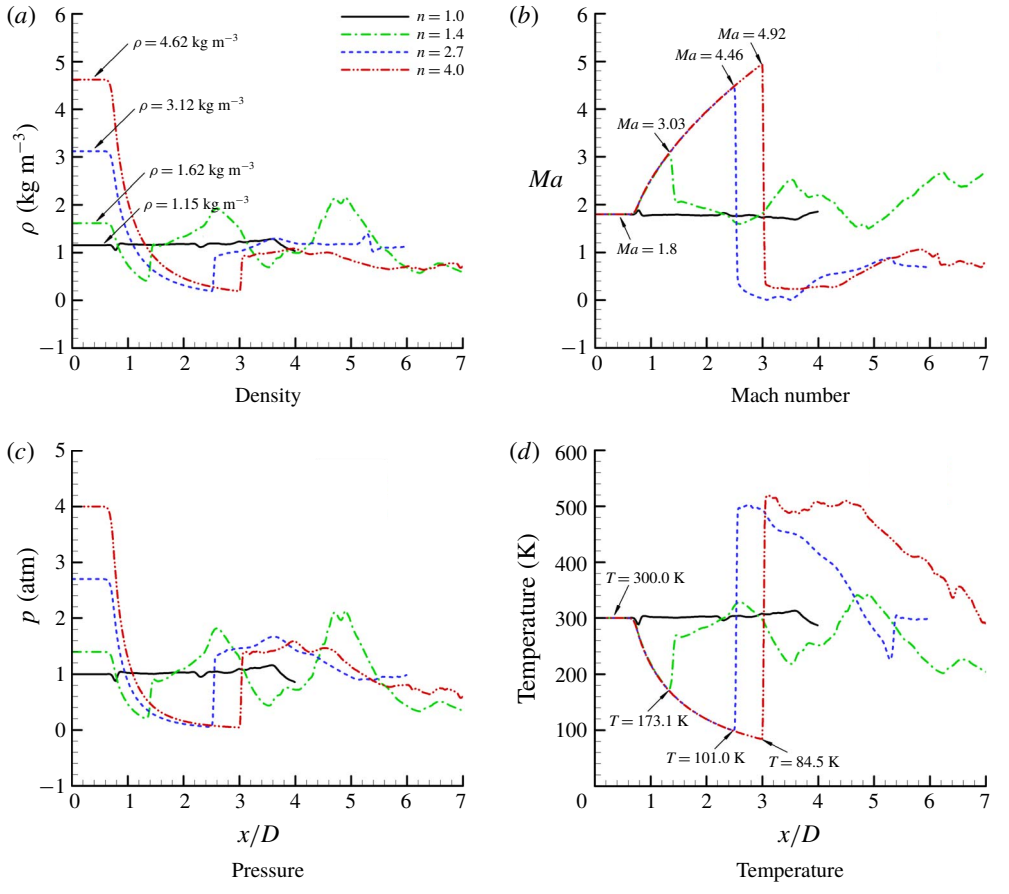

FIGURE 8. (Colour online) Variations of the main flow parameters of different under-expanded circular jets along the nozzle centreline.

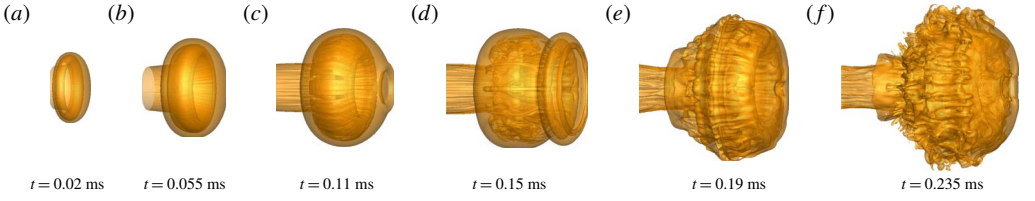

FIGURE 9. (Colour online) Sequential 3-D isosurface of the mixture fraction ($f = 0.83$) for $n = 1.4$.

generated from another slip line (Zhang *et al.* 2014), become more unstable since they locate closer to the primary vortex core and the vorticities are smaller. During the process of rolling over the periphery of the PVR, the SVRs break up and generate many fine-scale rib structures in the periphery of the PVR (figure 11*c*). These types of structures can be thought of as traces of the rib vortex in the fully developed state. As a result, the SVRs are difficult to identify from the interface of the PVR, as shown in figure 9(*f*).

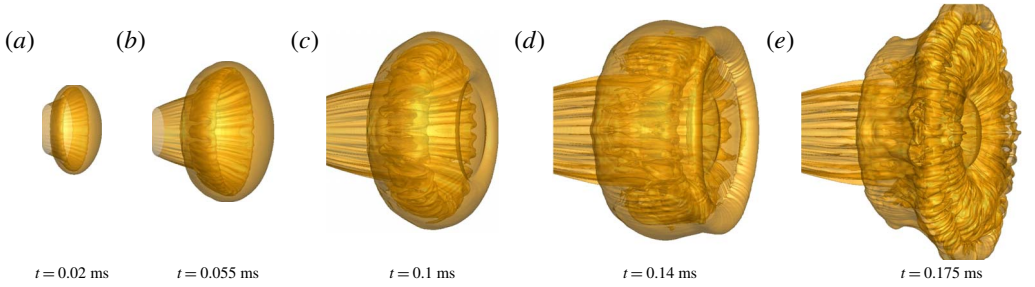

FIGURE 10. (Colour online) Sequential 3-D isosurface of the mixture fraction ($f = 0.83$) for $n = 4.0$.

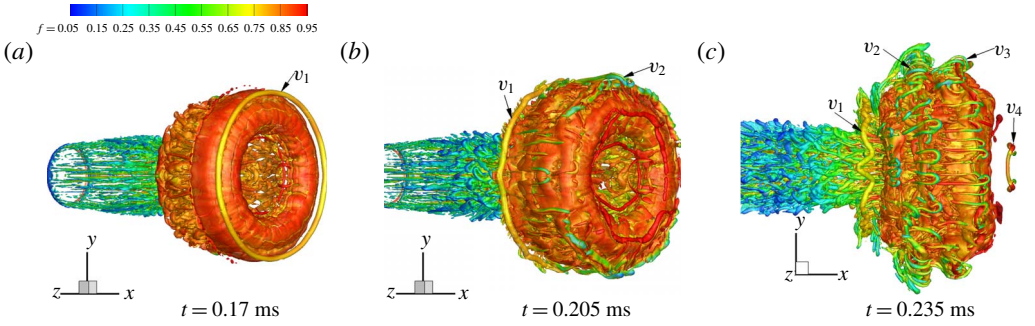

FIGURE 11. (Colour online) The 3-D isosurface of the second invariant of the velocity gradient tensor for the moderately under-expanded jet.

Since the expansion effect is augmented with an increase of the pressure ratio (n), the higher-pressure gas is accelerated to an even larger Mach number along its symmetric axis. Thus, the shape of the primary vortex core for the highly under-expanded jet is more prolate (figure 10*a*), and the waviness on the isomixture fraction surface of the vortex core appears earlier due to the stronger interaction of the vortex-induced shock wave with the vortex shear layer. Therefore, the 'halo vorticity' occupies the surrounding outer core region (figure 12*a*), which is consistent with the simulations of Archer, Thomas & Coleman (2008). It is also interesting to observe in figures 10 and 12 that the size and circulation of the secondary vortex core (V_1') gradually increase during its movement along the periphery of the PVR, which is markedly different from the ones in the moderately under-expanded jet.

The generation mechanism of the SVR for $n = 1.4$ has been described in Zhang *et al.* (2014); this mechanism is caused by the merging and shedding of two slip lines from the embedded shock. To illustrate the generation mechanism and evolution of the SVR for $n = 4.0$, the 3-D structural characteristics of the PVR during SVR formation are presented in figure 13, and the sequential vorticity ω_z and schlieren images of the symmetric plane during the evolution are shown in figure 14. The yellow layer in figure 13 shows the isosurface of the total vorticity, $\Omega = (\omega_x^2 + \omega_y^2 + \omega_z^2)^{1/2}$, and the grey layer is the shock interface. In figure 13(*a*), it is clear that an annular slip surface (S_1) is formed from the triple point of the Mach disc with a vorticity of opposite

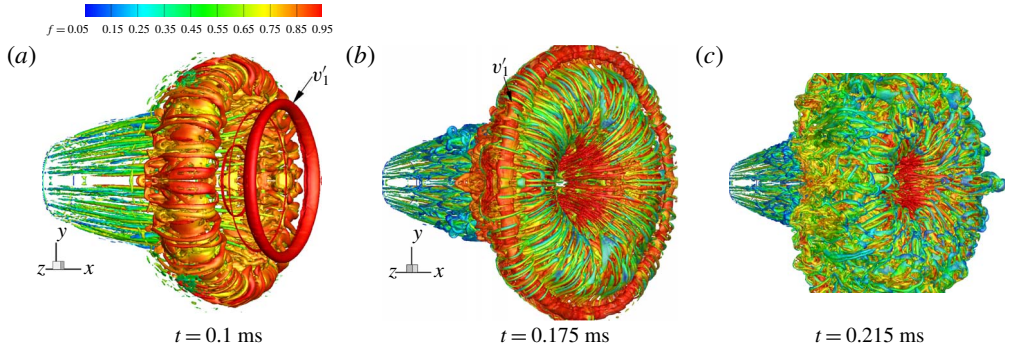

FIGURE 12. (Colour online) The 3-D isosurface of the second invariant of the velocity gradient tensor for the highly under-expanded jet.

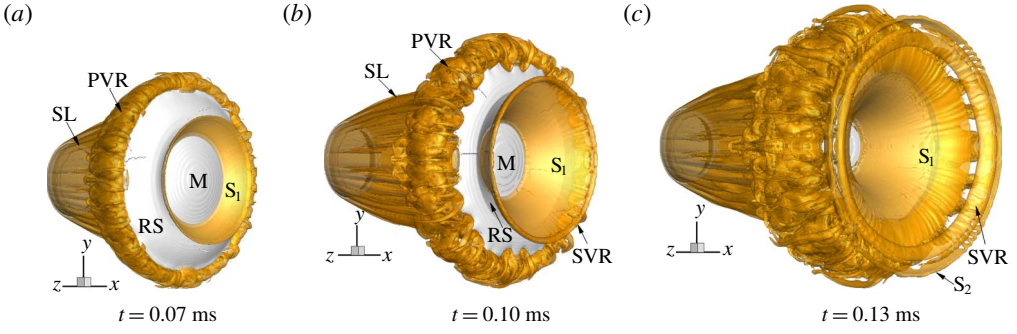

FIGURE 13. (Colour online) Isosurface of total vorticity ($\Omega = 5.0 \times 10^5$) showing the generation and evolution of the first SVR (V_1) for $n = 4.0$.

rotation to the jet shear layer (figure 14*a*), and its magnitude (figure 14*a*, $|\omega_z|_{max} = 1.015 \times 10^6$) is approximately equal to that of the jet shear layer ($|\omega_z|_{max} = 1.09 \times 10^6$).

In the initial stage, the slip surface is stable and smooth; however, there is a velocity difference on both its sides (figure 7*b*). Thus, the K–H instability exists. The slip surface loses stability under the effect of K–H instability during its spread, which leads to the rolling up of a SVR at its end (figure 13*b*,*c*). After generation, the SVR expands outwards, and the size and circulation of its core rapidly increase (figure 14) through the entrainment of the slip surface (S_1) and outsider gas, which leads to the generation of a new vortex-induced shock pair (SVS_1 and SVS_2) on opposite sides of the secondary vortex core, as shown at $t = 0.19$ ms of figure 14(*b*).

Since the gas velocity at the downstream of the Mach disc is subsonic (figure 7*b*), the flow velocity inside the slip surface is smaller than that outside. Hence, the vorticity of the SVR is large and opposite to that of primary vortex core (figure 14*a*). When the SVR interacts with the front of the PVR, the opposite induced velocity by the SVR locally decelerates the front interface and makes the convex leading front in the axial region change into the cap profile (figure 5*b*, CD). Later, the orbiting of the SVRs and the mutual interactions with the PVR make the flow of the front interface slow down and form a flat-faced structure (figure 10*d*,*e*). Subsequently, the trailing annulus slip surface is perturbed by the fluctuation in the turbulent PVR (figure 14*b*,

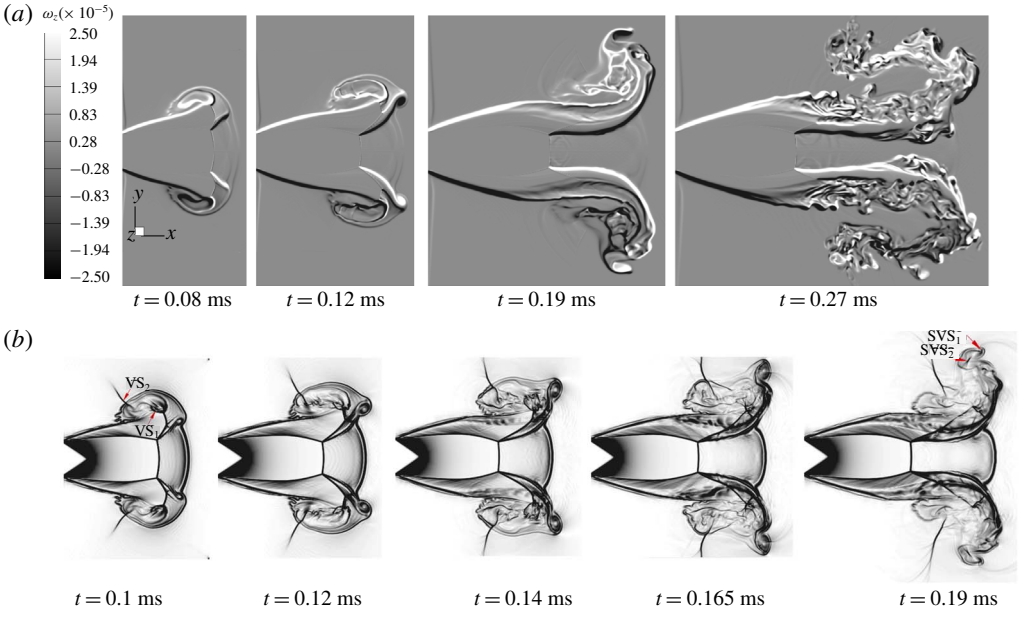

FIGURE 14. Sequential vorticity and schlieren images of the symmetric plane around the highly under-expanded jet ($n = 4.0$).

$t = 0.165$ ms; figure 13*c*), and finally a series of fine-scale vortex filaments are observed around the azimuth of the PVR (figure 12*b*).

As the SVR and trailing slip surface roll over the periphery of the PVR, the primary vortex core is stretched along the longitudinal direction (figure 14, $t = 0.19$ ms), and then compresses upstream and becomes highly turbulent after the SVR passes the vertex of the PVR (figure 14, $t = 0.27$ ms). Meanwhile, the trailing slip surface breaks up and forms coherent structures around the front interface of the PVR (figure 12*c*). From the colour distribution, the fine-scale coherent structures generated on the front interface of the PVR can improve the mixing effect.

Figures 15 and 16 present the head-on pressure contours of the cross-section of the primary vortex core at three different moments for $n = 1.4$ and 4.0. Figures 15(*a*) and 16(*a*) show that the region with the lowest pressure (blue) refers to the primary vortex core, which divides the flow fields with two high-pressure concentric rings. The exterior boundary of the outer loop denotes the precursor shock wave, while the inner boundary refers to the jet shear layer. At $t = 0.03$ ms, it is clear that the cross-flow field of the core appears completely symmetric and uniform in a circular shape for both $n = 1.4$ and 4.0, and the flow is laminar at this moment. Since the PVR expands and attenuates rapidly, most of the ambient gas is entrained into the core, which makes the diameter of its vortex core increase greatly. Meanwhile, the PVR becomes unstable (figures 15 and 16*b*), and the inner region of the core is distorted. At $t = 0.225$ ms, the radial profile of the pressure becomes random (figures 15 and 16*c*).

On the other hand, the PVR for $n = 4.0$ expands and attenuates more rapidly. Even the PVR transits from laminar to turbulent flow after $t = 0.15$ ms (figure 16*b*,*c*). Additionally, the pressure within jet centre is still high, and the ring is basically a circle; however, clouds with tiny vortices are included at $t = 0.225$ ms (figure 16*c*).

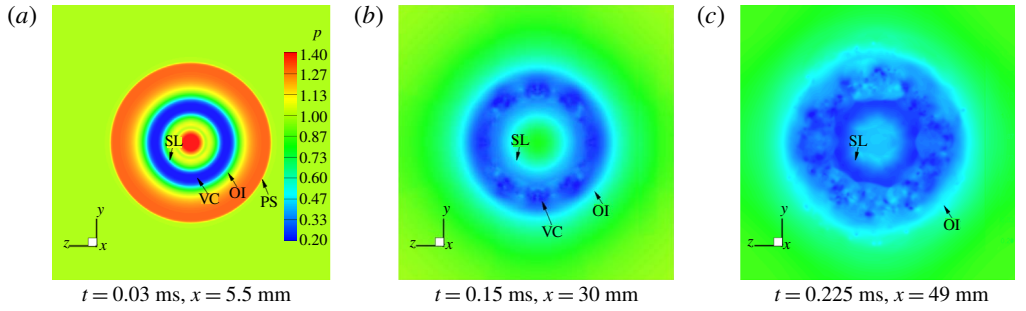

FIGURE 15. (Colour online) Head-on pressure contours of the PVR for the moderately under-expanded jet, $n = 1.4$. (SL, shear layer; VC, primary vortex core; OI, outer interface; PS, precursor shock wave.)

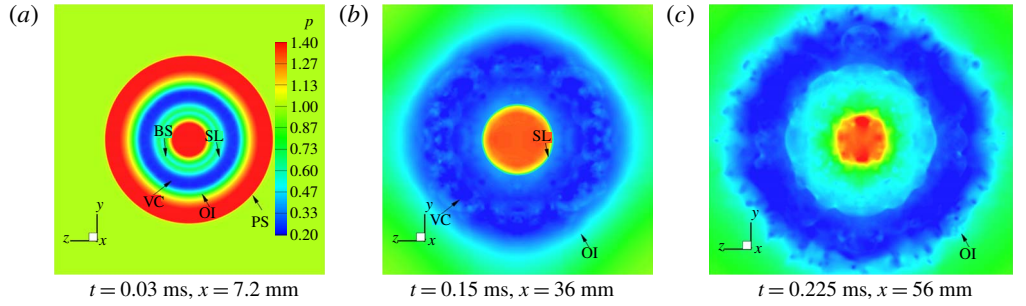

FIGURE 16. (Colour online) Head-on pressure contours of the PVR for the highly under-expanded jet, $n = 4.0$. (BS, barrel shock.)

3.3. *Instability analysis of the PVR*

To investigate the initial instabilities of the compressible vortex ring, the contours of the azimuthal vorticity (ω_θ) on a plane across the primary vortex core with $n = 1.4$ are shown in figure 17. This indicates that, at the initial stage ($t = 0.02$ ms), there is no obvious distortion near the inner and outer boundary of the ring. Along the radial direction, there exists one vorticity peak corresponding to the first radial mode, and the thin annulus near the outer boundary is the interface of the PVR; along the azimuthal direction, small distortions have appeared within the vortex core, which is different from the phenomenon observed by Ran & Colonius (2009) under a low Mach number, where the distortions appear near both the ring boundaries and the vorticity peak and no obvious small distortion has appeared. The difference can be attributed to the following two factors in our work: one is that there is no initial perturbation added and the other is the appearance of the vortex-induced shock pair at high Mach number, which interacts with the PVR and accelerates the instability of the vortex core (Zhang *et al.* 2015). As time goes on ($t = 0.055$ ms), the instability within the vortex core increases, and the radial vorticity develops two peaks illustrating the second radial mode (figure 17*b*). From $t = 0.11$ ms, the interface of the PVR starts to distort, and the flow becomes more unstable; finally, at $t = 0.225$ ms, the interface breaks into small vortices. In addition, it can also be observed that during the whole process of the morphology change of the vortex ring, the contours in the

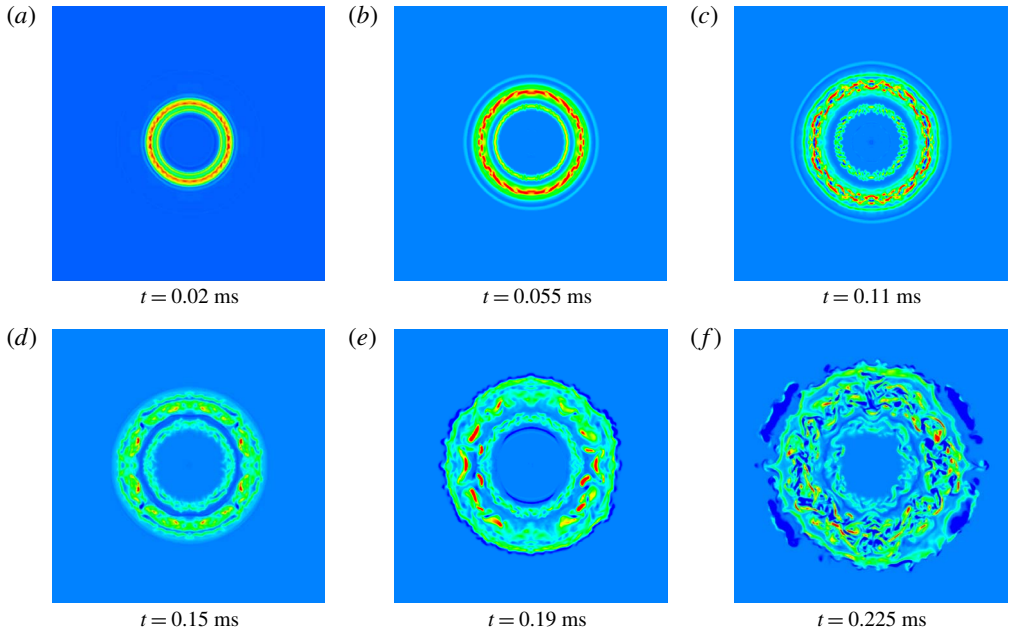

FIGURE 17. (Colour online) Contours of the azimuthal vorticity (ω_θ, S^{-1}) on a plane across the PVR core with contour levels: (*a*) max $= 10^6$, min $= -10^5$, level $= 109$; (*b–f*) max $= 7 \times 10^5$, min $= -10^5$, increment $= 109$. The pressure ratio is $n = 1.4$.

inner region of the ring remain at an almost constant size due to the continuous incoming flow from the nozzle, while the counters near the outer boundary expand outward.

Figure 18 displays the end view of the contours of the azimuthal vorticity with different radial and azimuthal modes at $t = 0.02$ ms, where r and j represent the number of the radial and azimuthal modes, respectively. Each row shares the same radial mode. It should be noticed that in the current work, a continuous 0.02 ms inflow is equivalent to a stroke length of approximately $L/D = Ma \times c \times t/D = 1$, where Ma is the Mach number, c is the speed of sound and D is the radius of the nozzle. Figure 18 indicates that, except for the first azimuthal mode, an even azimuthal mode shows a comparatively higher vortex intensity, which should be related to the harmonic effect of the azimuthal mode. For all the modes shown in figure 18, the radial mode 2 and azimuthal mode 8 show the highest intensity; and for the third radial mode, the azimuthal mode 12 shows the highest intensity. For each radial mode, its dominant azimuthal mode is determined by checking all azimuthal modes with the radial mode fixed. According to the heuristic linear instability model (Widnall & Tsai 1977; Saffman 1978; Ran 2004), a particular azimuthal number is unstable only for a certain radial mode. The unstable azimuthal mode can be calculated as $j = kR/\sigma$, where k is a constant and R and σ are the radius of the core and the ring (see the definitions of R and σ in figure 5). For radial modes 2 and 3, the values of the corresponding k are 2.5 and 4.35 (Widnall & Tsai 1977; Saffman 1978; Ran 2004). In the current case, for the second radial mode, $j = 2.5 \times 3 = 7.5$, which roughly coincides with the dominant mode shown in figure 18; furthermore, for the third radial mode the azimuthal mode 12 shows the highest intensity, which is also

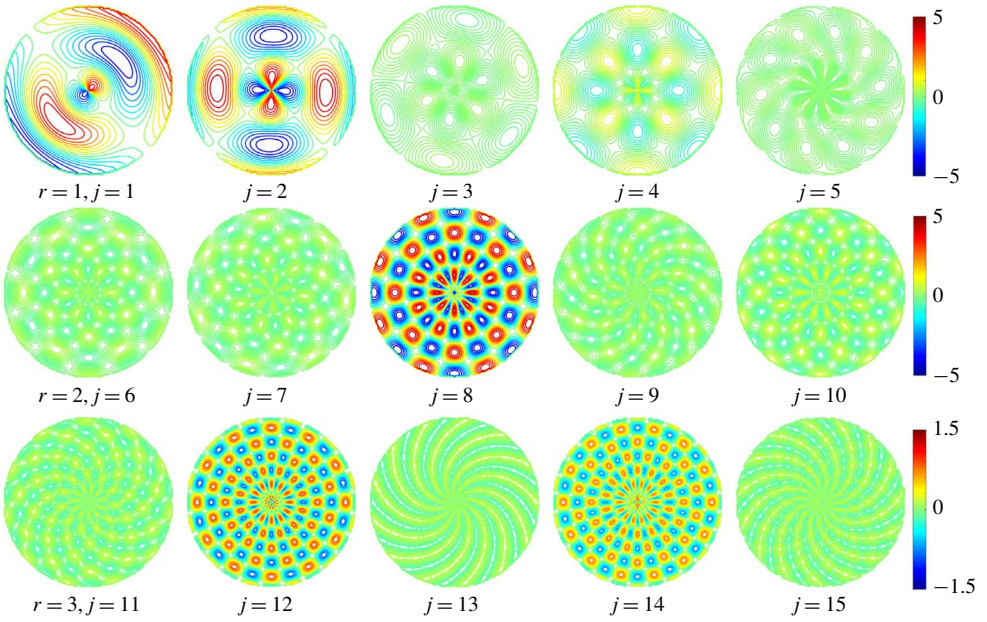

FIGURE 18. (Colour online) End view of the contours of the azimuthal vorticity with different radial and azimuthal modes at $t = 0.02$ ms. Each row has the same radial mode (r), and j represents the number of the azimuthal mode. The pressure ratio is $n = 1.4$. The unit of the scale bar is $10^3\,\mathrm{S}^{-1}$.

close to the calculated dominant mode number, $j = 4.35 \times 3 = 13.05$. It should be pointed out that the linear instability model for calculating the dominant azimuthal mode was developed by considering an inviscid incompressible flow (Widnall & Tsai 1977; Saffman 1978).

Figure 19 shows the end view of the contours of the azimuthal vorticity under different azimuthal modes with a radial mode of 3, at $t = 0.225$ ms. Different from the situation of 0.02 ms, the intensity of the vorticity of the different azimuthal modes does not show an obvious difference, and an even azimuthal mode no longer always has a higher intensity than an odd one. Such a difference should be attributed to the higher instability at 0.225 ms. Figure 20 displays the end view of the contours of the azimuthal vorticity with different radial and azimuthal modes at $t = 0.02$ ms, when the pressure ratio is 4.0. We found the dominant azimuthal modes are similar to those for the pressure ratio of 1.4. The intensity of the azimuthal mode increases as the pressure ratio becomes larger, but the difference is not significant, especially for the case with a radial number of 2, while the variation of the intensity of the one-dimensional azimuthal energy spectra is very large (see figure 22*b*,*c*). The similarity of the dominant modes may be attributed to the high-Mach-number flow in the current study; the initial instability is mainly caused by the interaction between the shock pair and the shear layer of the PVR. Figure 21 shows the end view of the contours of the azimuthal vorticity with different radial and azimuthal modes at different time steps when the pressure ratio is 4.0. Similar to the case of $n = 1.4$, as time proceeds, the difference of the intensity between different azimuthal modes decreases, and the even mode is no longer dominant compared with the odd mode.

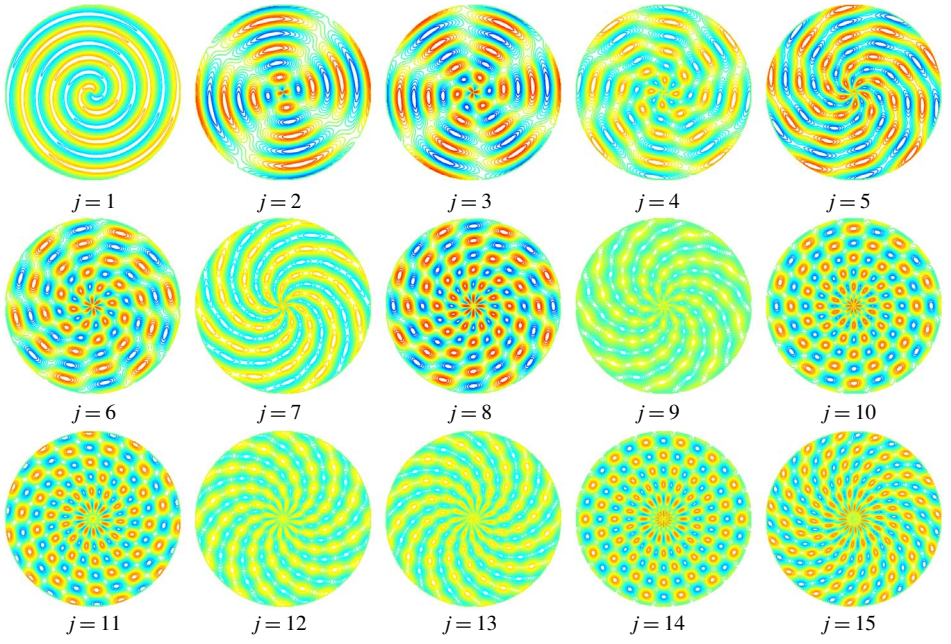

FIGURE 19. (Colour online) End view of the contours of the azimuthal vorticity with different radial and azimuthal modes at $t=0.225$ ms. The pressure ratio is $n=1.4$. The maximum and minimum contour levels are 2×10^4 and $-2\times10^4\,\mathrm{S}^{-1}$.

To study the turbulent transition of the flow, figure 22 plots the normalized azimuthal kinetic energy and the one-dimensional energy spectra along the θ direction at different times for both $n=1.4$ and 4.0. The azimuthal energy spectra are integrated (averaged) along the radial direction. As the flow initiates, the azimuthal kinetic energies of both cases have the same increasing tendency until $t=0.02$ ms, then the energy almost becomes constant for $n=1.4$; after $t=0.055$ ms, its growth becomes rapid, indicating that the flow instability increases. At $t=0.225$ ms, the azimuthal kinetic energy maintains an obvious rising trend, which implies a further increase of flow instability and flow transition to turbulence. For the curve of $n=4.0$, after approximately 0.02 ms, the normalized azimuthal kinetic energy becomes obviously higher, implying a higher level of azimuthal instability and turbulent transition; compare figure 22(*b*,*c*) for additional information. Furthermore, except in the initial period, the growth rate of $n=4.0$ is higher. Figure 22(*b*) shows that at the beginning of the flow, the energy concentrates at large-scale modes (small wavenumbers), and the modes with higher wavenumbers contain little energy. As time increases, the energies of all modes increase, indicating energy transfer from the mean flow; additionally, the higher azimuthal modes are excited obviously due to the nonlinear interaction between the lower modes. Corresponding to figure 22(*a*), at $t=0.225$ ms, the energy of the high azimuthal modes still tends to increase, implying that the flow is undergoing turbulence transition. Figure 22(*c*) shows that for the case of $n=4.0$ at 0.02 ms, the modes with higher wavenumbers have been excited, and after 0.15 ms, the development of the energy spectra has slowed down; this outcome has also been captured by the curve in figure 22(*a*). In addition, it can be noticed that figure 22(*b*) does not show distinct peaks corresponding to the azimuthal modes of 2, 8 and 12

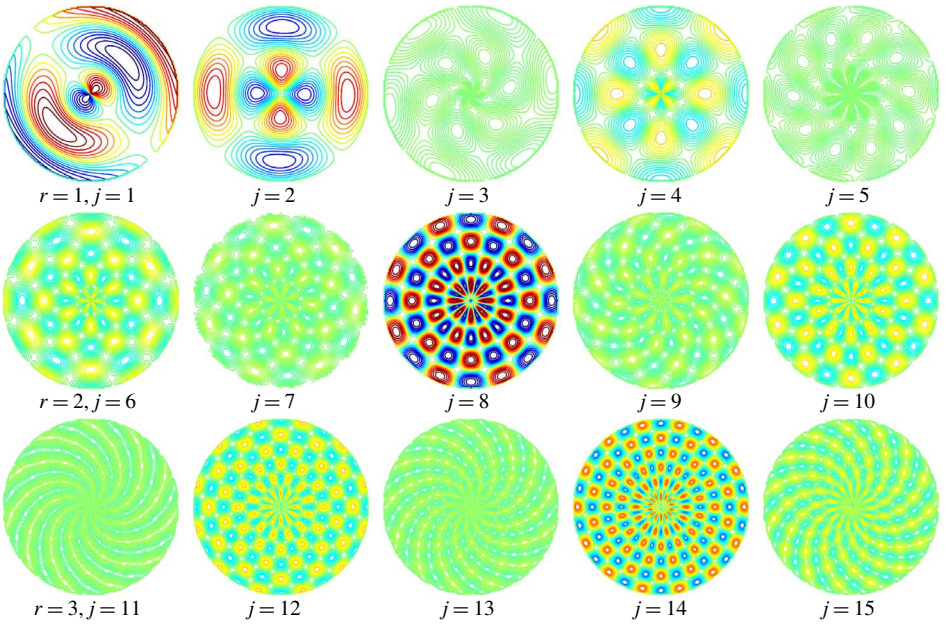

FIGURE 20. (Colour online) End view of the contours of the azimuthal vorticity with different radial and azimuthal modes at $t = 0.02$ ms. Each row has the same radial mode (r), and j represents the number of the azimuthal mode. The pressure ratio is $n = 4.0$. The maximum and minimum contour levels are 1×10^4 and $-1 \times 10^4\,\mathrm{S}^{-1}$.

displayed in figure 18, because the azimuthal kinetic energy analysed in figure 22(*b*,*c*) is integrated over the radius; thus, it refers to the azimuthal component solely.

3.4. *Geometric and mixing characteristics of the jet*

Figure 23 displays the trajectories of the first SVRs for both jets. Since the first SVRs eventually become unstable, the plot only shows their stable propagating process. It is clear that both SVRs have almost the same moving tendency (figure 23*a*), but for $n = 4.0$ there is a stronger transverse expanding effect and larger diameter than for $n = 1.4$ due to the higher inner pressure (figure 23*c*). After formation, the SVR moves mainly downstream (towards the front of the PVR); the axial distance from the tube exit to the SVR for both jets increases linearly at the early stage ($t^* = tUe/D > 6.6$) and then becomes slow and reaches the largest value as the SVR passes over the vertex of the PVR. After that, for $n = 1.4$, its SVR moves upstream and the corresponding axial distance decreases (figure 23*b*). On the other hand, the transverse expansions of the secondary vortex core for both jets increase first, and the growth gradient becomes large at the stage of the SVR moving along the head interface of the PVR, but the growth rate for $n = 4.0$ is much higher, and its SVR becomes unstable during the interaction with the PVR. However, for $n = 1.4$, the SVR loses its stability after its interaction with the PVR, and the diameter decreases at this time (figure 23*c*).

Figure 24 shows the time history of the axial distances of the PVR from the tube exit to its front interface (Lm) with different pressure ratios. It is clear that, first, Lm increases linearly and becomes nonlinear later. The linear stage is longer for smaller

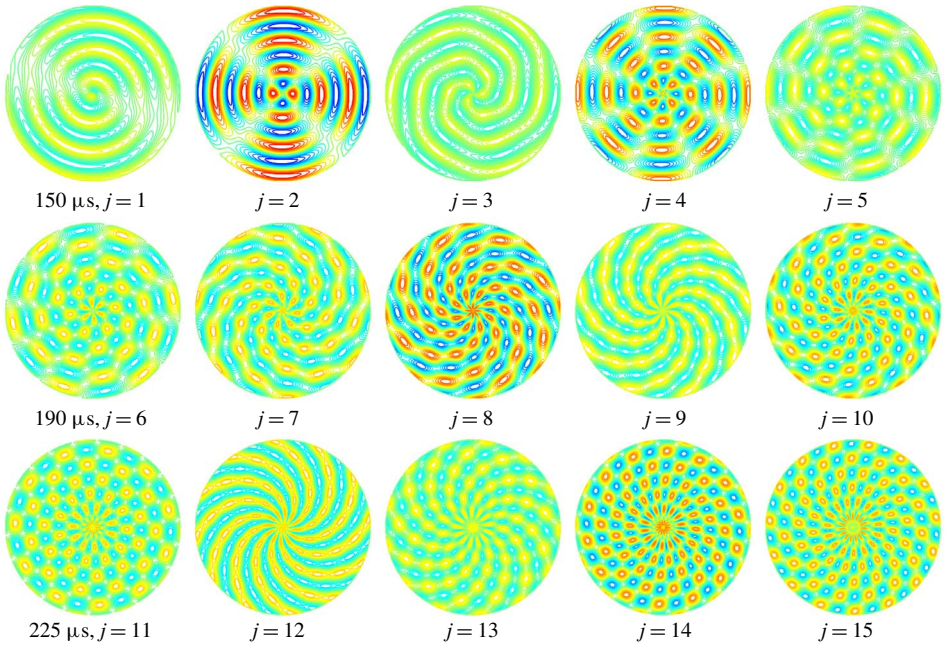

FIGURE 21. (Colour online) End view of the contours of the azimuthal vorticity with different radial and azimuthal modes at different time steps. Each row shares the same time. The pressure ratio is $n = 4.0$. The maximum and minimum contour levels are 2×10^4 and $-2 \times 10^4\ \mathrm{S}^{-1}$.

pressure ratio ($n = 1.0$ and 1.4) than for higher pressure ratio ($n = 2.7$ and 4.0). While for the highly under-expanded jet ($n = 2.7$ and 4.0), *Lm* increases rapidly first, due to the expanding effect of the jet flow, and then becomes slow (after $t^* = tU/D = 3.8$) under the action of the SVR; finally, the value of *Lm* for $n = 1.4$ exceeds that for $n = 2.7$ and 4.0 at $t^* = 9.1$ and 12.8, respectively.

Figure 25 shows the time history of unsteady jet entrainment rates (Zhang *et al.* 2018). Since the mixing process in the unsteady jet involves bulk mixing driven by a large-scale vortex ring, and smaller-scale mixing is dominated by turbulent coherent structures, the variation of the entrainment rate is actually determined by the stability of the PVR.

From figure 25, it is clear that the variations of the entrainment rates for both jets have the same tendency. They decrease first at the early stage ($t \leqslant 0.02$ ms) due to the relative stability of the jet flow; at this time, the entrainment gas mass is smaller than the added jet mass from the nozzle. However, with the loss of stability of the PVR, the entrainment mass increases and becomes larger than the added gas mass, making the entrainment rate rise at a relatively small rate during the period of 0.02 ms $\leqslant t \leqslant$ 0.20 ms for $n = 1.4$ and 0.02 ms $\leqslant t \leqslant 0.17$ ms for $n = 1.4$. Finally, the increase rates of both jets grow quickly along with the turbulence transition of the PVR ($t \geqslant 0.20$ ms for $n = 1.4$, and $t \geqslant 0.17$ ms for $n = 4.0$) due to its interaction with the SVRs.

On the other hand, the value of the entrainment rate for $n = 4.0$ is smaller than that for $n = 1.4$ at the initial stage, but its gradient increase is larger. For $n = 4.0$, the vorticity of its SVR is much larger than that for $n = 1.4$; therefore, its action with the PVR is stronger. In addition, its trailing slip surface makes the front interface of the

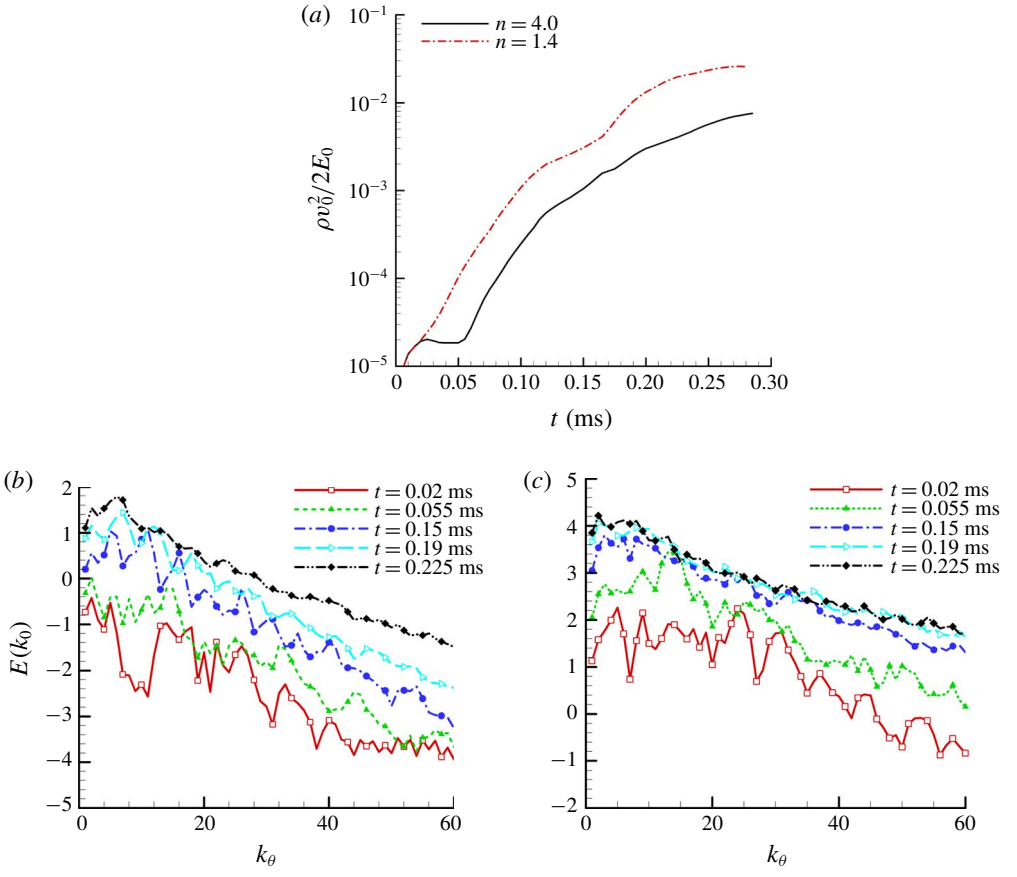

FIGURE 22. (Colour online) (*a*) Time evolution of the normalized azimuthal kinetic energy, where $(1/2)\rho v_\theta^2$ and E_0 are the azimuthal kinetic energy and total energy, respectively. (*b*) One-dimensional energy spectra along the θ direction at different times for $n = 1.4$. (*c*) One-dimensional energy spectra along the θ direction at different times for $n = 4.0$. Parameter k_θ is the azimuthal wavenumber along the angular direction and the wavelength is $\lambda = 2\pi/k_\theta$.

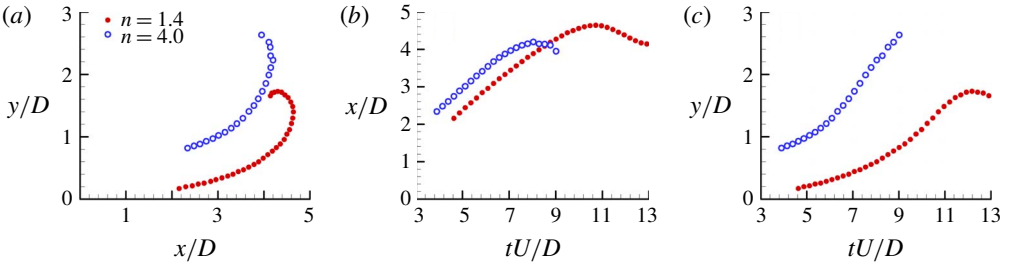

FIGURE 23. (Colour online) Trajectories of the first SVRs.

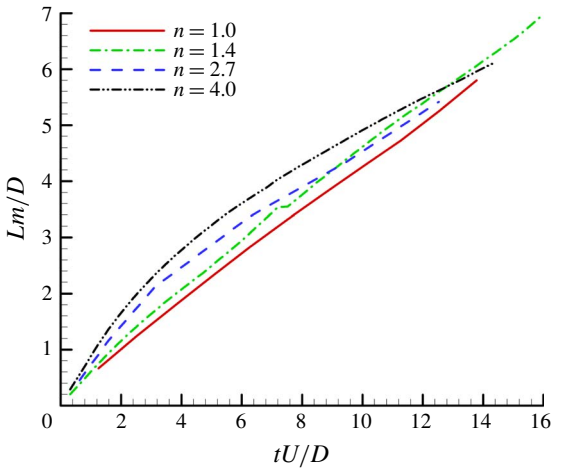

FIGURE 24. (Colour online) Time history of Lm for different pressure ratios.

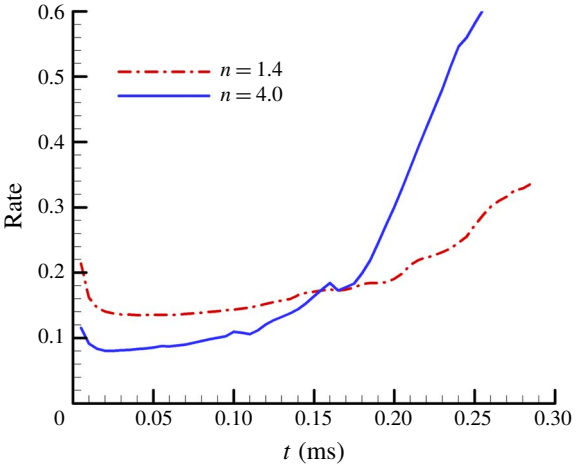

FIGURE 25. (Colour online) Time history of the entrainment rate for both $n = 1.4$ and 4.0.

PVR change dramatically. Under the action of both the above effects, the entrainment rate increases more rapidly and becomes larger than that for $n = 1.4$ after $t > 0.164$ ms. This indicates that the development of the SVR for the highly under-expanded jet flow has a great effect on enhancing the mixing effect.

4. Conclusions

The initial 3-D flow structures of moderately and highly under-expanded circular jets have been numerically investigated. The main initial flow structures of both jets include the precursor shock wave, PVR, Mach cone, SVR and vortex-induced shock pair, but their shock wave structures are different. For $n = 1.4$, the shock wave regular reflection appears within the jet and a typical shock cell generates behind the PVR; for $n = 4.0$, the reflection transits to Mach reflection and the Mach disc structure emerges, and we find that the outsider end of the annular slip surface originates from the triple

point of the Mach disc, which rolls up to generate the SVR under the effect of K–H instability.

For both jets ($n = 1.4$ and 4.0), during jet evolution, there are two main factors to accelerate the instability of the PVR: one is the interaction of the shock pair with the vortex core and the other is the interaction of the SVR with the PVR. The former is in action all the time and causes the PVR to lose its stability starting from the vortex core, and the latter operates only when the SVR rolls over the periphery of the PVR, and its effect increases with the growth of the pressure ratio.

The characteristics of the SVR are also under the influence of the pressure ratio. For $n = 1.4$, its size is stable, and the interaction is dominated by the PVR; then, it loses stability after rolling over the periphery of the PVR and turns into irregular waviness at the wake. The subsequent SVRs break up into many fine-scale rib structures on the periphery of the PVR. For $n = 4.0$, it has a strong transverse expansion, and its size and circulation also increase during the evolution, and the shock pair appears within its core. Furthermore, its action causes the PVR and itself to distort and become unstable immediately.

The radial and azimuthal modes for $n = 1.4$ obtained by Fourier analysis indicate that for the second and third radial modes, the dominant azimuthal modes are the eighth and twelfth modes, which are close to the unstable azimuthal modes calculated by the heuristic linear instability model (Widnall & Tsai 1977; Saffman 1978; Ran 2004); and it is also found that the high and moderate pressure ratios show similar dominant azimuthal modes, implying that for both cases, the initial instability may be attributed to the interaction between the shock pair and the shear layer of the PVR. The azimuthal energy spectra show that at the initial stage, only the small wavenumbers are excited; as flow develops, the higher azimuthal modes are excited obviously, indicating the flow transition to turbulence. Furthermore, as the pressure ratio increases, the development of the energy spectra becomes faster.

Finally, we compare the axial distances of the PVR (L_m) for both jets and find that they increase linearly and then become nonlinear for both jets, the duration for the linear stage being longer for the small pressure ratio ($n = 1.0$ and 1.4). Additionally, since the vorticity of the SVR for $n = 4.0$ is much larger than that for $n = 1.4$, its action and its trailing slip surface cause the front interface of the PVR to change dramatically. As a result, the SVR for the highly under-expanded jet flow has a stronger effect on enhancing the mixing effect.

Acknowledgements

This work was supported by the National Natural Science Foundation of China (grant nos. 11502117 and 11702005) and the Foundation of Key Laboratory of Transient Physics (614260403041802).

Appendix. Numerical validation by several supersonic jet problems

Here, we show a further validation of our numerical model by simulation and compare the simulation results with the corresponding experimental results, which we have published previously (Zhang *et al.* 2014, 2017). In addition to the inflow conditions, all of the following simulation cases were using the same numerical method and computational model as this paper.

Figure 26 shows the evolution process of the initial flow field of the moderately under-expanded circular jet with the corresponding experimental results of Murugan & Das (2010). The experimental sequence images were obtained using a double-pulsed

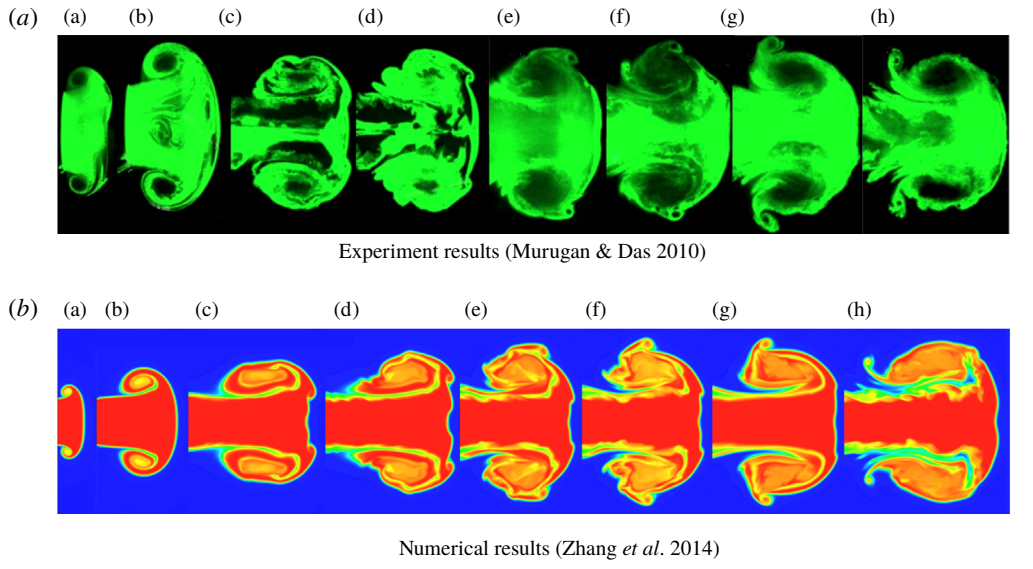

FIGURE 26. (Colour online) Comparison of the vortex ring evolution process of our computational results ($Ma = 1.4$) with the corresponding experimental results ($Ma = 1.7$) of Murugan & Das (2010).

laser and a high-speed CCD camera for $Ma = 1.7$, and our numerical results (Zhang *et al.* 2014) are the mixture fraction contours for $Ma = 1.4$ and $n = 1.4$. Both types of omages show the detailed evolution of the PVRs and SVRs and agree well with each other; however, due to the different Mach numbers and expanding pressure ratios, some particular differences exist between them.

Figure 27 compares the instantaneous flow fields of our numerical images (Zhang *et al.* 2014) with the experimental images of Zare-Behtash *et al.* (2008*a*,*b*). The experimental Mach number is $Ma = 1.31$, and our numerical images are obtained from the superimposition of the schlieren results of the symmetric section with the 3-D isosurface of the jet flow mixture fraction. It is obvious that the shape and position of both the SVR and PVR of our computational results ($Ma = 1.4$) are also in good agreement with experimental images of Zare-Behtash *et al.* (2008*a*,*b*). The SVRs are formed even for low Mach numbers of $Ma = 1.4$ and 1.31 rather than a critical Mach number of $Ma \geqslant 1.6$ mentioned in (Murugan & Das 2010). The roll up of the vortices along the shear layer and their engulfment into the main vortex core can be clearly seen in both the numerical and experimental results, which will be discussed in the following paragraphs.

The instantaneous flow structure of an under-expanded elliptic jet on the minor plane (Zhang *et al.* 2017), in which the elliptic jet's axis ratio a/b equals 2.5, is compared with the corresponding experimental results of Zare-Behtash *et al.* (2009*a*,*b*), as shown in figure 28. The Mach number and nozzle pressure ratio of our schlieren results are $Ma = 1.4$ and $n = 1.4$, while the experimental Mach number is $Ma = 1.32$ (figure 28*b*). It is shown in figure 28 that both the shock patterns and vortex structures of our numerical results are in good agreement with the corresponding experimental schlieren images (Zare-Behtash *et al.* 2009*a*,*b*).

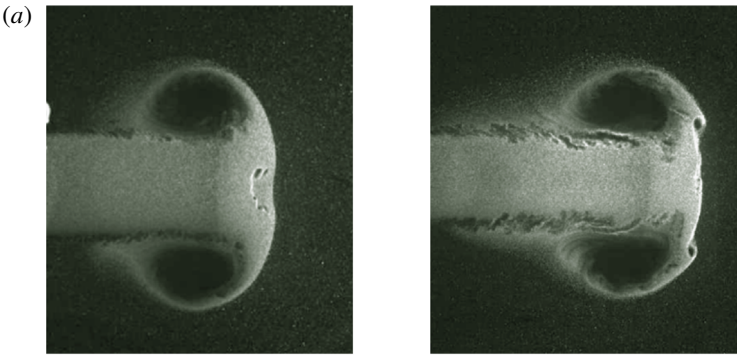

Experimental PIV results (Zare-Behtash, Kontis & Takayama 2008)

Numerical results (Zhang *et al*. 2014)

FIGURE 27. (Colour online) Comparison of the instantaneous flow fields of our numerical images (Zhang *et al.* 2014) with the experimental images of Zare-Behtash *et al.* (2008*a*,*b*).

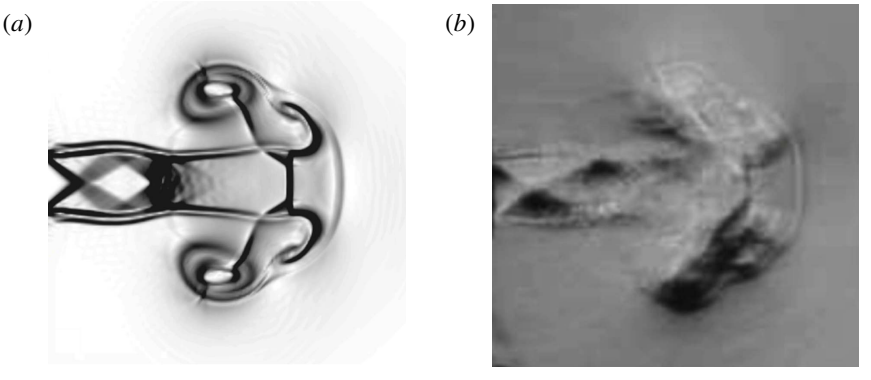

Numerical Schlieren image (Zhang *et al*. 2017)

Experimental Schlieren of Zare-Behtash *et al*. (2009)

FIGURE 28. Comparison of the experimental and numerical schlieren images of an unsteady elliptic jet with an axis ratio of $a/b = 0.4$.

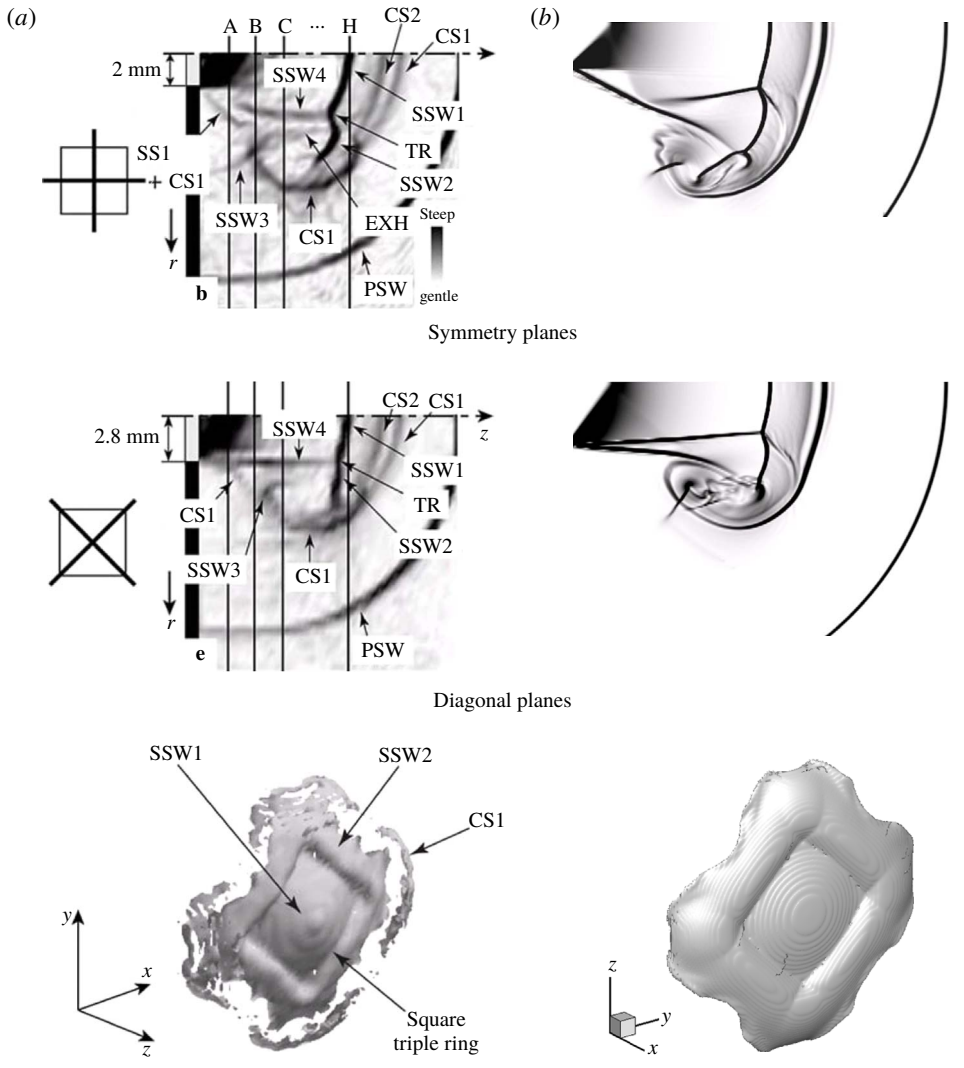

Pseudo-schlieren CT images of Maeno *et al*. (2005)

Numerical schlieren images (Zhang *et al*. 2017)

FIGURE 29. Comparison of the instantaneous flow field of our numerical images (Zhang *et al.* 2017) with the pseudo-schlieren CT images of Maeno *et al.* (2005). (CS, contact surface; EXH, expansion head; PSW, primary shock wave; SS, slip surface; SSW, secondary shock wave; TR, triple ring.)

Figure 29 presents the instantaneous flow structures of a highly under-expanded square jet (Zhang *et al.* 2017) with the corresponding experimental results of Maeno *et al.* (2005). The jet Mach number and nozzle pressure ratio of our schlieren results are $Ma = 1.4$ and $n = 4.4$, while the incident shock Mach number of the experimental results is $Ma = 2.2$. It is obvious that the shock wave structures, contact surface and other shape density fronts on both symmetry and diagonal planes in our computational results agree well with experimental images in Maeno *et al.* (2005). Additionally, the

3-D shape of the Mach disc is also in accordance with the experimental images of Maeno *et al.* (2005).

REFERENCES

ARCHER, P. J., THOMAS, T. G. & COLEMAN, G. N. 2008 Direct numerical simulation of vortex ring evolution from the laminar to the early turbulent regime. *J. Fluid Mech.* **598**, 201–226.

ARAKERI, J. H., DAS, D., KROTHAPALLI, A. & LOURENCO, L. 2004 Vortex ring formation at the open end of a shock tube: a particle image velocimetry study. *Phys. Fluids* **16**, 1008–1019.

BERGER, M. & COLELLA, P. 1989 Local adaptive mesh refinement for shock hydrodynamics. *J. Comput. Phys.* **82**, 64–84.

BROUILLETTE, M., TARDIF, J. & GAUTHIER, E. 1995 Experimental study of shock-generated vortex rings. In *Shock Waves @ Marseille IV*, pp. 361–366. Springer.

BROUILLETTE, M. & HEBERT, C. 1997 Propagation and interaction of shock-generated vortices. *Fluid Dyn. Res.* **21**, 159–169.

COLONIUS, T., LELE, S. K. & MOIN, P. 1994 Scattering of sound waves by a compressible vortex: numerical simulations and analytical solutions. *J. Fluid Mech.* **260**, 271–298.

DEITERDING, R., CIRAK, F., MAUCH, S. P. & MEIRON, D. I. 2007 A virtual test facility for simulating detonation- and shock-induced deformation and fracture of thin flexible shells. *Intl J. Multiscale Comput. Engng* **5**, 47–69.

DONALDSON, C. D. & SNEDEKER, R. S. 1971 A study of free jet impingement. Part 1. Mean properties of free and impinging jets. *J. Fluid Mech.* **45**, 281–319.

HAMZEHLOO, A. & ALEIFERIS, P. G. 2016 Gas dynamics and flow characteristics of highly turbulent under-expanded hydrogen and methane jets under various nozzle pressure ratios and ambient pressures. *Intl J. Hydrogen Energy* **41**, 6544–6566.

HILLIER, R. 1991 Computation of shock wave diffraction at a ninety degrees convex edge. *Shock Waves* **1**, 89–98.

HILL, D. J. & PULLIN, D. I. 2004 Hybrid tuned center-difference-WENO method for large eddy simulations in the presence of strong shocks. *J. Comput. Phys.* **194**, 435–454.

HILL, D. J., PANTANO, C. & PULLIN, D. I. 2006 Large-eddy simulation and multiscale modeling of a Richtmyer–Meshkov instability with re-shock. *J. Fluid Mech.* **557**, 29–61.

HUNT, J. C. R., WRAY, A. A. & MOIN, P. 1988 Eddies, streams, and convergence zones in turbulent flows. In *Proc. 1988 Summer Program of the Center for Turbulence Research*, pp. 193–207.

ISHII, R., FUJIMOTO, H., HATTA, N. & UMEDA, Y. 1999 Experimental and numerical analysis of circular pulse jets. *J. Fluid Mech.* **392**, 129–153.

KITAJIMA, S., IWAMOTO, J. & TAMURA, E. 2009 A study on the behavior of shock wave and vortex ring discharged from a pipe. In *10th International Conference on Fluid Control, Measurements, and Visualization, August 17–21, Moscow, Russia*.

KOSOVIC, B., PULLIN, D. I. & SAMTANEY, R. 2002 Subgrid-scale modeling for large-eddy simulations of compressible turbulence. *Phys. Fluids* **14**, 1511–1522.

LI, H. Z., JIANG, X. H., WANG, Y. & GUO, Z. Q. 2015 *Intermediate Ballistics*. Beijing Institute of Technology Press.

LOMBARDINI, M., HILL, D. J., PULLIN, D. I. & MEIRON, D. I. 2011 Atwood ratio dependence of Richtmyer–Meshkov flows under reshock conditions using large-eddy simulations. *J. Fluid Mech.* **670**, 439–480.

LUNDGREN, T. S. 1982 Strained spiral vortex model for turbulent fine structure. *Phys. Fluids* **25**, 2193–2203.

MAENO, K., KANETA, T., MORIOKA, T. & HONMA, H. 2005 Pseudo-schlieren CT measurement of three-dimensional flow phenomena on shock waves and vortices discharged from open ends. *Shock Waves* **14**, 239–249.

MARIANI, R., QUINN, M. K. & KONTIS, K. 2013 A note on the generation of a compressible vortex rings using helium as driver gas. *Proc. Inst. Mech. Engrs Part G* **227**, 1637–1645.

MATSUDA, T., VUORINEN, V., YU, J., TIRUNAGARI, S., KAARIO, O., LARMI, M., DUWIG, C. & BOERSMA, B. J. 2013 Large-eddy simulation of highly under-expanded transient gas jets. *Phys. Fluids* **25**, 016101.

MISRA, A. & PULLIN, D. I. 1997 A vortex-based subgrid stress model for large-eddy simulation. *Phys. Fluids* **9**, 2443–2454.

MINOTA, T. 1998 Shock/vortex interaction in a flow field behind a shock wave emitted from a shock-tube. In *Proceedings of the 2nd International Workshop on Shock Wave/Vortex Interaction*, pp. 149–160. International Shock Wave Institute.

MURUGAN, T. & DAS, D. 2010 Characteristics of counter-rotating vortex rings formed ahead of a compressible vortex ring. *Exp. Fluids* **49**, 1247–1261.

MURUGAN, T., DE, S., DORA, C. L., DAS, D. & PREM KUMAR, P. 2013 A study of the counter rotating vortex rings interacting with the primary vortex ring in shock tube generated flows. *Fluid Dyn. Res.* **45**, 025506.

PANTANO, C., DEITERDING, R., HILL, D. J. & PULLIN, D. I. 2007 A low numerical dissipation patch based adaptive mesh refinement method for large-eddy simulation of compressible flows. *J. Comput. Phys.* **221**, 63–87.

PULLIN, D. I. 2000 A vortex-based model for the subgrid flux of a passive scalar. *Phys. Fluids* **12**, 2311–2319.

RAN, H. & COLONIUS, T. 2009 Numerical simulation of the sound radiated from a turbulent vortex ring. *Aeroacoustics* **8**, 317–336.

RAN, H. 2004 Numerical study of the dynamics and sound generation of a turbulent vortex ring. PhD thesis, California Institute of Technology, Pasadena, CA.

SAFFMAN, P. 1978 The number of waves on unstable vortex rings. *J. Fluid Mech.* **84**, 625–639.

WIDNALL, S. & TSAI, C. 1977 The instability of the thin vortex rings of constant vorticity. *Phil. Trans. R. Soc. Lond.* A **287**, 273–305.

ZARE-BEHTASH, H., KONTIS, K. & GONGORA-OROZCO, N. 2008*a* Experimental investigation of compressible vortex loops. *Phys. Fluids* **20**, 126105.

ZARE-BEHTASH, H., KONTIS, K. & TAKAYAMA, K. 2008*b* Compressible vortex loops studies in a shock tube with various exit geometries. *AIAA Paper* 2008-362.

ZARE-BEHTASH, H., KONTIS, K., GONGORA-OROZCO, N. & TAKAYAMA, H. 2009*a* Compressible vortex loops: effect of nozzle geometry. *Intl J. Heat Fluid Flow* **30**, 561–576.

ZARE-BEHTASH, H., GONGORA-OROZCO, N. & KONTIS, K. 2009*b* Global visualization and quantification of compressible vortex loops. *J. Vis.* **12**, 233–240.

ZARE-BEHTASH, H., KONTIS, K., GONGORA-OROZCO, N. & TAKAYAMA, K. 2010 Shock wave-induced vortex loops emanating from nozzles with singular corners. *Exp. Fluids* **49**, 1005–1019.

ZHANG, H. H., CHEN, Z. H., JIANG, X. H. & LI, B. M. 2011 Numerical investigations on the thrust augmentation mechanisms of ejectors driven by pulse detonation engines. *Combust. Sci. Technol.* **183**, 1069–1082.

ZHANG, H. H., CHEN, Z. H., JIANG, X. H. & LI, H. Z. 2013 Investigations on the exterior flow fields and the efficiency of the muzzle brake. *J. Mech. Sci. Technol.* **27**, 95–101.

ZHANG, H. H., CHEN, Z. H., LI, B. M. & JIANG, X. H. 2014 The secondary vortex rings of a supersonic under-expanded circular jet with low pressure ratio. *Eur. J. Mech. (*B*/Fluids)* **46**, 172–180.

ZHANG, H. H., CHEN, Z. H., JIANG, X. H. & HUANG, Z. G. 2015 The starting flow structures and evolution of a supersonic planar jet. *Comput. Fluids* **114**, 98–109.

ZHANG, H. H., CHEN, Z. H., GUO, Z. Q. & SUN, X. H. 2017 Characteristic behavior of shock pattern and primary vortex loop of a supersonic square jet. *Intl J. Heat Mass Transfer* **115**, 347–363.

ZHANG, H. H., CHEN, Z. H., GUO, Z. Q., ZHENG, C. & XUE, D. W. 2018 Numerical investigation on the three-dimensional flow characteristics of unsteady subsonic elliptic jet. *Comput. Fluids* **160**, 78–92.